Title

Impact of Local Structure in Supported CaO Catalysts for Soft-Oxidant-Assisted Methane Coupling Assessed through Ca K–Edge X–ray Absorption Spectroscopy

Authors

Filardi, Leah R

Vila, Fernando D

Hong, Jiyun

et al.

Peer reviewed

Article

Impact of Local Structure in Supported CaO Catalysts for Soft-Oxidant-Assisted Methane Coupling Assessed through Ca K-Edge X-ray Absorption Spectroscopy

Leah R. Filardi, Fernando D. Vila, Jiyun Hong, Adam S. Hoffman, Jorge E. Perez-Aguilar, Simon R. Bare, Ron C. Runnebaum,* and Coleman X. Kronawitter*

ACCESS | Metrics & More | Article Recommendations | SI Supporting Information

ABSTRACT: Soft-oxidant-assisted methane coupling has emerged as a promising pathway to upgrade methane from natural gas sources to high-value commodity chemicals, such as ethylene, at selectivities higher than those associated with oxidative (O_2) methane coupling (OCM). To date, few studies have reported investigations into the electronic structure and the microscopic physical structure of catalytic active sites present in the binary metal oxide catalyst systems that are known to be effective for this reaction. Correlating the catalyst activity to specific active site structures and electronic properties is an essential aspect of catalyst design. Here, we used X-ray absorption spectroscopy at the Ca K-edge to ascertain the most probable local environment of Ca in the ZnO-supported Ca oxide catalysts. These catalysts are shown here to be active for N_2O-assisted methane coupling (N_2O-OCM) and have previously been reported to be active for CO_2-assisted methane coupling (CO_2-OCM). X-ray absorption near edge structure features at multiple Ca loadings are interpreted through simulated spectra derived from *ab initio* full multiple scattering calculations. These simulations included consideration of CaO structures organized in multiple spatial arrangements—linear, planar, and cubic—with separate analyses of Ca atoms in the surfaces and bulk of the three-dimensional structures. The morphology of the oxide clusters was found to influence the various regions of the X-ray absorption spectrum differently. Experiment and theory show that for low-Ca-loading catalysts (≤1 mol %), which contain sites particularly active for methane coupling, Ca primarily exists in an oxidized state that is consistent with the coordination environment of Ca ions in one- and two-dimensional clusters. In addition to their unique nanoscale structures, the spectra also indicate that these clusters have varying degrees of undercoordinated surface Ca atoms that could further influence their catalytic activities. The local Ca structure was correlated to methane coupling activity from N_2O-OCM and previously reported CO_2-OCM reactor studies. This study provides a unique perspective on the relationship between the catalyst physical and electronic structure and active sites for soft-oxidant-assisted methane coupling, which can be used to inform future catalyst development.
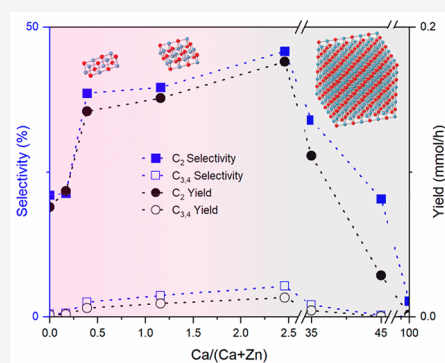
1. INTRODUCTION

There has been a recent surge in natural gas development, and the U.S. Department of Energy expects continual growth for at least the next several decades.[1] Natural gas is often a byproduct of oil extraction[2] in low-population areas which poses a major economic challenge for gas transportation.[3] As a result, it is often flared into carbon dioxide or released, emitting greenhouse gases to the atmosphere.[2] Roughly 90% of the end-use of natural gas is combustion for heat or energy, further adding carbon dioxide to the atmosphere.[4] Upgrading methane, the dominant chemical species present in natural gas, into a more energy-dense chemical or fuel would allow for a more efficient utilization of this abundant resource and help to reduce greenhouse gas emissions.

Oxidative coupling of methane (OCM) is a highly explored avenue of methane upgrading to larger hydrocarbons via C−C bond formation.[5] However, the presence of strong oxidant species at high temperatures leads to a strong trade-off between methane conversion and C_2 product selectivity[6] where undesirable combustion reactions of methane and C_2 products limit product yields below 30%.[7] However, the use of softer oxidants that do not form gas-phase oxygen species offers an opportunity to break the trade-off relationship. Carbon dioxide and nitrous oxide are both emerging oxidants to replace oxygen during OCM.[8−11] C_2 product selectivity over 80% can easily be achieved with binary metal oxide catalysts, notably when coupling a basic oxide with a reducible oxide.[12−14]

This cooperation has been demonstrated by previous efforts to characterize these binary oxide catalysts. For many bulk reducible metal oxides including MnO_2,[15] CeO_2,[14] CoO, CuO, Bi_2O_3, and Fe_2O_3,[16] XRD and XPS[17] have demonstrated their partial reduction after reaction. Reaction in the absence of any oxidant leads to complete reduction,[13] indicating CO_2- and N_2O-OCM proceed through a Mars−van Krevelen mechanism where oxygen vacancies are formed during the reaction with methane and are replenished by the oxidant.[12] The presence of oxygen vacancies has been confirmed in PrO_2 via O_2-TPD.[18] Addition of a basic metal oxide can promote CO_2 chemisorption for increased conversion over the reducible sites during CO_2-OCM, demonstrated by CO_2-TPD.[12,19] Catalyst basicity and reducibility were also shown to correlate with C_2 product yields for N_2O-OCM.[20]

Recent work used CO_2-IR-TPD to establish a volcano relationship between catalyst basicity and CO_2-OCM performance.[21] The interface between basic and reducible metal oxides in a Ca/ZnO catalyst had the presence of medium-strength basicity and was proposed to be responsible for selective methane coupling. It was also observed that very low concentrations of calcium (~0.6 mol %) exhibited excellent catalytic performance, and the Ca sites had electronic and geometric properties that were not characteristic of bulk CaO species, according to various characterization methods, including Ca L-edge X-ray absorption near edge structure (XANES). However, the specific nature of these Ca species has not been thoroughly investigated.

X-ray absorption spectroscopy (XAS) is a useful tool for determining the local structure of metal oxide nanoparticles. Decreases in second and third shell coordination numbers, relative to bulk metal oxide, have been correlated to nanoparticles of defined sizes.[22,23] These results in tandem with DFT calculations have predicted specific structures of supported metal oxide clusters with 9−13 metal atoms.[24] There have been few studies that use Ca K-edge extended X-ray absorption fine structure (EXAFS) to inform on Ca-containing nanoparticle sizes and structure of highly dispersed[25,26] and nanoparticle Ca species.[27,28] Changes in Ca−O coordination can be observed during mineral crystallization as the solid phases become larger and more ordered.[29] Ca deposition on coal via impregnation and ion exchange yielded catalysts that lacked any Ca−Ca coordination due to a high degree of dispersion.[25] The aggregation of $CaCO_3$ and CaO species was observed after high-temperature treatments.

This work uses Ca K-edge XAS paired with theoretical XAS simulations to evaluate the local coordination environment of Ca species in Ca/ZnO catalysts over the wide range of Ca compositions previously studied[21] and correlate structure to CO_2-OCM and N_2O-OCM performance. The structure of low-Ca-loading catalysts is contrasted with that of bulk CaO species to reveal the presence of ultrasmall CaO clusters with one-dimensional linear and two-dimensional planar geometries. The difference in active site structure is associated with enhanced methane coupling performance for low-Ca-loading Ca/ZnO catalysts.

2. MATERIALS AND METHODS

2.1. Catalyst Synthesis.
Calcium carbonate (98% purity) and calcium hydroxide (98% purity) were acquired from VWR and Acros Organics, respectively. Calcium oxide−zinc oxide composite catalysts were prepared via a wet impregnation synthesis as described earlier.[21] Briefly, calcium nitrate tetrahydrate (99%, ACS Reagent, MP Biomedicals) was dissolved in Milli-Q (18 Mohm) water. Zinc oxide (99.9% metal basis, Alfa Aesar) was added, and the resulting slurry was sonicated and stirred partially covered overnight. The resulting white solids were dried at 120 °C for 24 h before being calcined in 50 mL/min air (zero air, Praxair) at 850 °C (ramp 5 °C/min) for 4 h. Henceforth, the Ca loading will be denoted by the resulting Ca/(Zn + Ca) ratio, or mol % of cation. Calcium oxide was synthesized by heating 100 mL of a 0.25 M calcium nitrate solution in an oil bath to 80 °C.[30] Under vigorous stirring, a 50 mL solution of 1 M NaOH was added dropwise, resulting in a cloudy solution of a white precipitate. The solids were vacuum filtered, washed with deionized water, and dried overnight at 120 °C before calcination (see above). Calcium weight loading was determined by ICP-OES (Table S2).

2.2. Materials Characterization.
Calcium K-edge XAS data were collected at beamline 4-3 of the Stanford Synchrotron Radiation Lightsource equipped with a double-crystal Si(111) monochromator at an orientation of $\Phi = 90°$. Helium was used as the ionization chamber gas with the ion chamber voltage at 200 V DC and negative polarity. To minimize absorption by air at these low photon energies, a UHP helium-purged tube was installed between the first ion chamber and the sample stage. The photon energy was initially calibrated with a Ti metal foil in transmission mode. The beamline was calibrated by defining the edge energy, the maximum if the first derivative of the Ti foil spectra, to 4966.0 eV. Subsequently, an initial reference spectrum of $CaCO_3$ was acquired where E_0 was observed to be 4037.6 eV. Measurements of $CaCO_3$ were repeated at least every 24 h, and E_0 was aligned to 4037.6 eV to account for any drift in the monochromator. Spectra were acquired between 3805.0 and 4645.0 eV. At least 4 spectra of each sample were acquired and merged to improve the signal-to-noise ratio. All data were collected in fluorescence mode. For calcium catalysts with ≤2 mol %, data were collected using a 7-element Canberra silicon-drift detector. For all other samples and standards, a PIPS detector was used. Approximately 1−3 mg of sample was ground to a fine powder and smeared as a thin uniform layer onto a zero-sulfur-containing adhesive tape and placed in an airtight cell inside a glovebox and then transferred to the beamline stage with helium flow.

Post-processing and analysis of the XAS data were performed using the Athena and Artemis software of the Demeter package.[31] Energy correction was applied from the corresponding $CaCO_3$ reference spectrum. The pre-edge region in the range of 43.4−20.0 eV below the edge was normalized with a linear fit and in the range of 50.0−400.0 eV above the edge with a second-order polynomial fit. The data were modeled in q-space to reduce any errors associated with fitted coordination numbers by filtering out high-frequency (scattering paths at longer R) components from the data. The data were fit in the q range of 3.4−9.1 Å^{-1}. The same k range and a back-Fourier transform R range of 1.0−3.5 Å was used. EXAFS models were built using scattering paths generated from CIF files using FEFF6. CIF files were downloaded from the Materials Project[32] and consisted of $Ca(OH)_2$ (mp-23879), CaO (mp-2605), and ZnO (mp-2133) where the central Zn atom was replaced with a Ca atom to simulate an isolated Ca atom within the ZnO lattice. The amplitude reduction factor S_0^2 was determined from a fit of 2 mol % Ca/

ZnO to be 0.73. For all catalysts, the Ca−O coordination number was fixed to 6. The continuous Cauchy wavelet transform (CCWT) analysis on the EXAFS data was done using Python codes based on Larch modules.[33] The analysis was performed on the k range of 3.4−9.1 Å^{-1} for CaO, 1 mol % Ca/ZnO, and 0.6 mol % Ca/ZnO EXAFS spectra. The k^2-weighted CCWT was calculated for the k range of 0−9.1 Å^{-1} and R range of 0.2−6.0 Å.

2.3. Computational Details. The XANES simulations were performed with FEFF10.[34−36] The SCF stage used a cutoff radius of 5 Å and maximum angular momenta of 3 and 2 for Ca and O, respectively. The FMS stage used a cutoff radius of 9 Å, with maximum angular momenta of 4 and 3 for Ca and O, respectively. These values ensured convergence for the bulk case. The model for the bulk CaO simulations was generated from the experimental structure[37] of CaO with space group $Fm\overline{3}m$ and lattice constant 4.8105 Å, resulting in a Ca−O bond distance of 2.405 Å. The model for Ca in the surface was generated by cleaving the bulk model in order to expose the (100) surface. In order to explore the effect on the XANES of a broad range of sizes, morphologies, and local environments for the CaO, which could vary as a function of loading, unsupported cluster models were generated by repeating the neutral Ca_4O_4 cubic unit along one, two, or three directions in order to generate "linear", "planar", and "cubic" clusters (as shown in the insets of Figure 4). These are labeled as (n,l,m) according to the number of cubic units in each direction. Based on the Ca−O and Ca−Ca bond distances obtained in the EXAFS fits and exploratory supported relaxations (see below), all of the model cluster structures retain the original, unrelaxed crystal structure. All calculations used the final state rule approximation for the core−hole and the default Hedin−Lundqvist approximation for the self-energy. The calculations also included room temperature thermal damping at the level of single scattering, using the correlated Debye model with a Debye temperature of 562 K. This temperature was chosen to match the fitted σ^2 for the Ca−O paths in the catalysts at 300 K. While the bulk and surface simulations were performed on a single representative Ca atom, for the (n,l,m) clusters the XANES calculations were performed for each Ca atom in the structure, and the resulting spectra were averaged to obtain the final result. The effect of dipole-forbidden transitions was studied by adding the MULTIPOLE card to the FEFF calculations to include the quadrupole contributions. In addition, the effect of s → d transitions were quantified by removing the s → p contributions from the total spectra. The theoretical spectra were normalized using a procedure similar to that used in EXAFS analysis in which the post-edge decay of the atomic background is removed. The difference between the XANES of the catalysts and that of bulk CaO (ΔXANES) was quantitatively compared to that of the (n,l,m) clusters and the theoretically simulated bulk CaO. This was done using a Frechet form figure of merit (FOM), described in detail in the Supporting Information. Finally, in order to investigate the suitability of unrelaxed, unsupported cluster models for the assessment of the changes in the XANES as a function of loading, a ZnO-supported CaO model was also constructed by creating an epitaxial contact[38] between the O surface of the (0001) plane of ZnO and the equivalent surface of the (111) plane in CaO, with the latter being contracted by 4.5% to match the ZnO surface.[37] From this structure, a pyramidal CaO cluster of side ~9 Å was carved to expose the (100) surfaces. The internal degrees of freedom (excluding the

bottom two layers of ZnO support) of the resulting simulation cell ($a = b = 19.497$ Å, $c = 25.0$ Å, $\alpha = \beta = 90.0°$, $\gamma = 120.0°$) were optimized with VASP using the PBE functional, a plane-wave cutoff of 400 eV, and PAW pseudopotentials (Figure S9). The supported structure expands laterally to release virtually all of the epitaxial contraction, resulting in an average bond distance of 3.40 Å, compared to the bulk CaO distance of 3.39 Å at this level of theory. This results in a bond strain index of 1.00 ± 0.01. The Ca−Ca scattering length distribution is narrow, with a static mean-square relative displacement (MSRD) of 3.6×10^{-3} Å^2. The Ca−Zn shell at 3.43 Å is highly disordered with a MSRD of 22.4×10^{-3} Å^2, which will be relevant to later discussions. The structural similarities between this supported, relaxed example and the rigid models described above justify the latter use in the general XANES simulations.

2.4. Catalytic Activity Measurements. N_2O-OCM experiments over a series of Ca loadings were conducted in a quartz downflow, packed-bed reactor with a 4 mm ID. A sample mass of 0.750 g was sieved between 250 and 425 μm and loaded into the tube, supported by quartz wool (Acros Organics). The reactor was heated in a tubular furnace at 5 °C min^{-1} to 800 °C under 13.3 mL min^{-1} argon (99.997%, Praxair) and then quickly cooled to 550 °C. Flow was then switched to bypass the reactor and adjusted to 3.3 mL min^{-1} methane (99.9995%, Matheson), 6.7 mL min^{-1} nitrous oxide (99.998%, Linde), and 3.3 mL min^{-1} argon prior to flow through the reactor. Reaction products were measured by an online Agilent 7890A gas chromatograph (GC) with a CP-SilicaPLOT column to quantify hydrocarbon species with FID and Porapak Q and ShinCarbon ST columns to quantify all other species with TCD. Separate N_2O-OCM experiments were performed as follows to determine activation energies. Activation energies were determined after verification that the reactor was in a differential regime. A sample mass of 0.2 g and a total flow rate of 30 mL min^{-1} with varying feed ratios were used. The reactor was heated in a tubular furnace at 5 °C min^{-1} to 800 °C under 13.3 mL min^{-1} argon and then quickly cooled to 520 °C. Flow was then switched to bypass the reactor and stabilize for 45 min. The reactor temperature was held for 2.5 h while injecting to the GC, then quickly ramped by 10 °C, and held for another 2.5 h. This proceeded from 520 to 560 °C. Steady-state data over the 2.5 h period were averaged.

3. RESULTS AND DISCUSSION

3.1. Evaluation of Ca K-Edge XANES and Pre-Edge Structure. The XANES spectra of Ca/ZnO catalysts with varying concentrations of Ca are compared to common bulk Ca reference compounds—CaO, $Ca(OH)_2$, and $CaCO_3$ in Figure 1. The overall shape of the spectra of all Ca/ZnO catalysts resembles that of CaO, with the white line absorption centered at 4046.8 eV and a significant shoulder feature at 4037.9 eV. Spectra of catalysts with 2 mol % and higher Ca content are nearly identical with that of CaO, indicating that Ca exists in its bulk oxide phase in these higher Ca-loaded catalysts (Figure S1). This is consistent with XRD, TEM, and L-edge XANES results, published in prior work.[21] Below 2 mol % Ca content, the shoulder feature diminishes, the white line peak decreases and broadens, a new pre-edge feature grows at 4034.3 eV, and post-edge oscillations are significantly dampened. These features resemble those seen in the spectrum of $Ca(OH)_2$, but rigorous EXAFS analysis verifies the absence
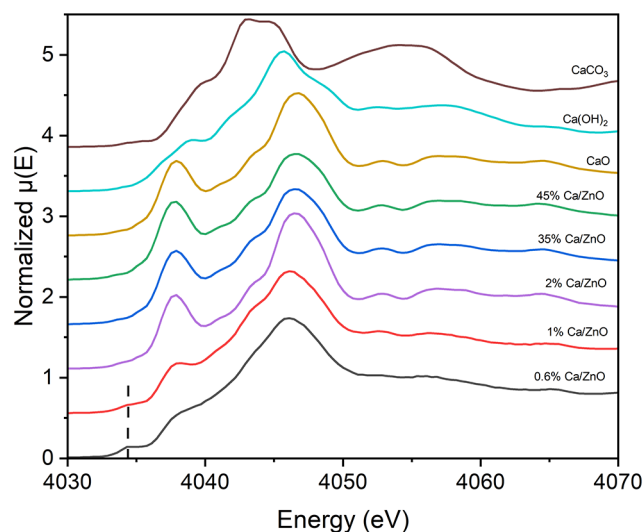
Figure 1. *Ex situ* Ca K-edge XANES spectra were collected at room temperature in He. The dashed line is to visualize the pre-edge feature. Spectra are offset for clarity.

Figure 2. Magnitudes of the Fourier transforms of phase-uncorrected k^2-weighted EXAFS of low-Ca-loading Ca/ZnO catalysts using the k range of 3.4–9.1 Å^{-1}.

of a hydroxide phase; XAS associated with the hydroxide phase is addressed later. The new pre-edge feature is present only in the two lowest Ca-loading catalysts. Several different physical assignments of this peak have been reported.[39,40] Theoretical simulations of Ca local density of states, provided later in this report, provide justification for assigning this peak to a Ca 1s to p electronic transition.

3.2. Characterization of CaO Structure by EXAFS Analysis. Modeling of the EXAFS spectra provides information on the local structure of dispersed Ca sites present in the low-Ca-loading catalysts—1 and 0.6 mol % Ca/ZnO. To determine the precise Ca coordination environment, a q-space fit was used[41] to filter out high-frequency components to quantify observed changes in specifically the first two scattering paths (see the Methods section for more details). At high Ca composition, self-absorption[42] distorts the data for >2 mol % Ca, which prevents EXAFS analysis of those catalysts. The 2 mol % Ca/ZnO catalyst was reported to contain CaO particles >40 nm in size, determined by XRD.[21] This sample has well-defined XAS features that demonstrate the absence of the self-absorption effects observed with higher Ca loadings. Combined, these results reinforce our assumption that the Ca speciation in 2 mol % Ca/ZnO catalyst is equivalent to that of bulk CaO. Thus, the 2 mol % Ca/ZnO catalyst was used to determine the value of S_0^2, 0.73 (Figure S2 and Table S3), which is consistent with a previously reported value of 0.8.[43]

The magnitudes of the Fourier transforms of the EXAFS spectra for the low-Ca-loading catalysts are shown in Figure 2. The first peak is comparable in intensity across the three catalysts. The 1 and 0.6 mol % Ca/ZnO catalysts exhibit a significant decrease in all peak intensities at distances beyond 2.4 Å. Path analysis of CaO (Figure S3) shows that the first peak is associated with Ca–O at a bonding distance of 2.42 Å and the second peak is only associated with Ca–Ca single scattering at a distance of 3.42 Å. These results suggests that at loadings ≤1 mol % the Ca oxide exists as nanoparticles significantly smaller than those in the higher-Ca-loading catalysts; we henceforth refer to the ultrasmall Ca oxide structures in the two low-Ca-loading catalysts as clusters.
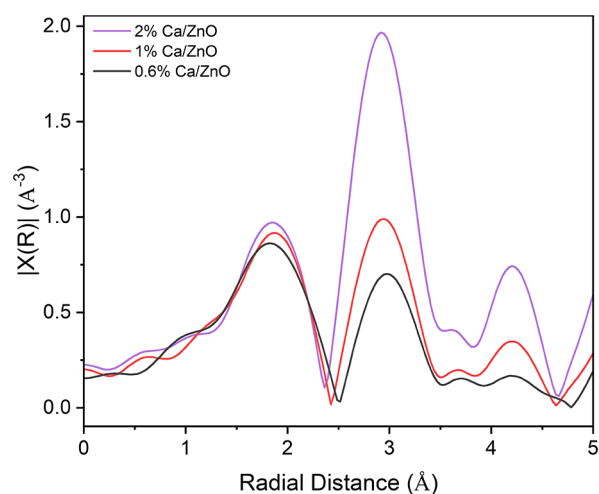
The two low-Ca-loading catalysts were modeled with the Ca–O and Ca–Ca scattering paths of bulk CaO. The Ca–O coordination was first allowed to float but always converged to a value close to 6. In subsequent models, it was fixed to 6 to simplify the model. This is a safe assumption because the first shell peak intensity in R-space is equivalent to the 2 mol % Ca/ZnO reference, and isolated Ca atoms have been reported to maintain a bulk Ca–O coordination number for the nearest-neighbor coordination.[25] The fitting results are listed in Figure 3 and Table 1. The data of the high-Ca-loading catalysts are
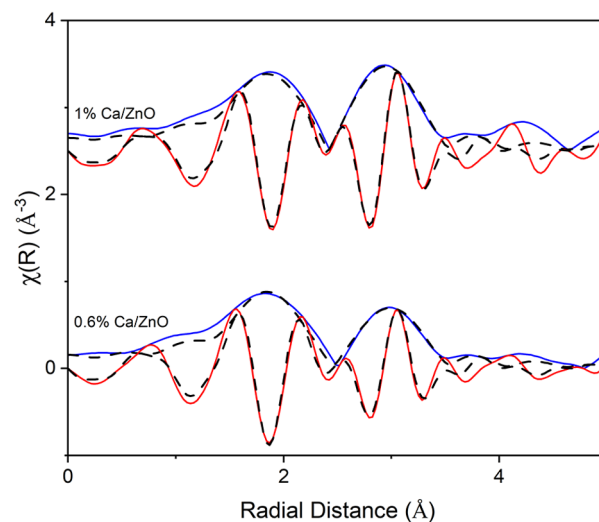

Figure 3. Magnitudes and imaginary portions of the k^2-weighted R-space functions for spectra associated with the low-Ca-loading catalysts are shown using solid blue and red lines, respectively; fits are shown with dashed lines. The data were back-Fourier transformed in the R range of 1.0–3.5 Å and fit in the q range of 3.4–9.1 Å^{-1}.

presented in the R-, q-, and k-spaces in Figure S4 without fits. All fits result in oxygen and calcium distances associated with bulk CaO with little to no increases in the σ^2. The lack of difference in the Ca–O bond length and degree of disorder supports a similar coordination number to that of bulk CaO.[44] This is consistent with reports that Ca nanostructures undergo

Table 1. Best Fit of the EXAFS Parameters for Ca/ZnO Catalysts[a]

	path	CN	R (Å)	$\sigma^2 \times 10^3$ (Å²)	ΔE_0 (eV)	R-factor	S_0^2
1% Ca/ZnO	Ca−O	6	2.37 ± 0.01	6.1 ± 1.6	0.8 ± 1.0	0.0111	0.73
	Ca−Ca	5.9 ± 0.4	3.41 ± 0.01	4.6			0.73
0.6% Ca/ZnO	Ca−O	6	2.36 ± 0.02	6.7 ± 1.9	1.6 ± 1.8	0.0347	0.73
	Ca−Ca	4.1 ± 0.7	3.42 ± 0.03	4.6			0.73
Simulated CaO clusters	Ca−O[b]		2.41				
	Ca−Ca[c]		3.40				

[a]Notation: CN, coordination number; S_0^2, amplitude correction term; ΔE_0, energy correction factor; R, scattering path length; σ^2, disorder term. A k range of 3.4−9.1 Å⁻¹ and an R range of 1.0−3.5 Å were used. Values without error bounds were held constant. [b]The CN of the Ca−O scattering paths cannot be directly compared to experimental results because the Ca atoms on the surface of the simulated structures were uncapped rather than oxygen-terminated. [c]The CN of the Ca−Ca scattering paths range from 4.0−4.7, 5.3−7.0, and 6.8−9.2 for the linear, planar, and cubic theoretical clusters, respectively.
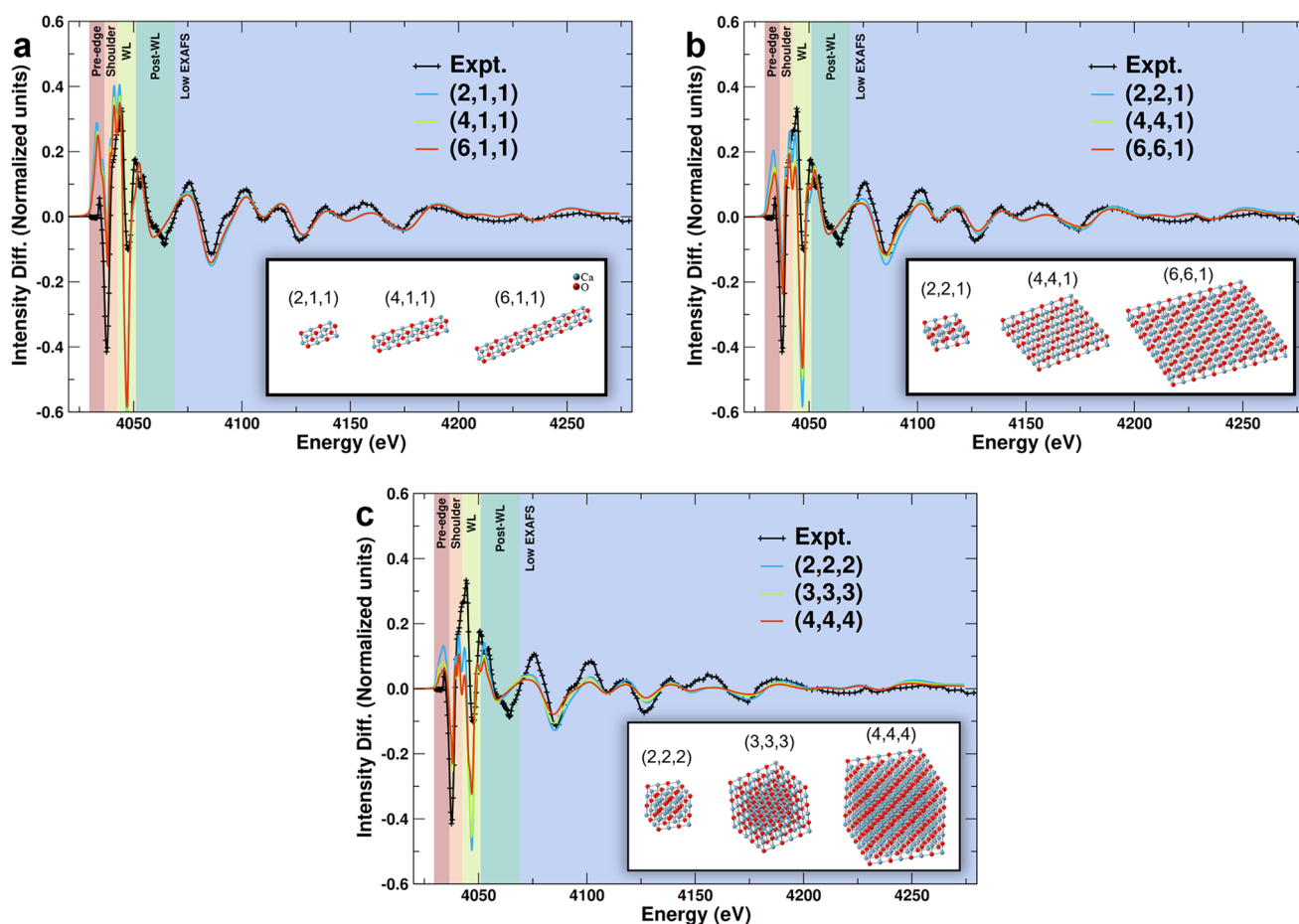

Figure 4. Difference between the experimental spectra of 0.6 mol % Ca/ZnO and CaO reference compared to the difference between simulated spectra of CaO nanoparticles of varying sizes and bulk CaO for the (a) linear, (b) planar, and (c) cubic morphologies. The numbers in parentheses represent the number of Ca₄O₄ units in each dimension. The CN of the Ca−Ca scattering path ranges from 4.0−4.7, 5.3−7.0, and 6.8−9.2 for the linear, planar, and cubic theoretical clusters, respectively.

negligible lattice distortion and maintain rigidity.[45,46] The Ca−Ca coordination numbers are 5.9 ± 0.4 and 4.1 ± 0.7 for the 1 and 0.6 mol % Ca/ZnO catalysts, respectively. These values are significantly smaller than the bulk CaO Ca−Ca coordination number of 12, indicating that calcium exists as nanoparticles of decreasing size.[22,47] Structural disorder could also lead to a reduction of long-range coordination but would predominately influence the third and higher shells.[22] The Ca−O and Ca−Ca scattering distances remain within error of those of bulk CaO, indicating that little to no CaO lattice distortion occurs with a

decreasing cluster size. This finding simplifies the theoretical modeling by allowing for the use of unrelaxed structures in the XANES simulations.

A Ca−Zn scattering path cannot be quantifiably modeled from the EXAFS data. While the data can be fit with a Ca−Zn scattering path, the resulting σ^2 and ΔE_0 values are unrealistically large (Figures S5, S6 and Tables S4, S5). Figure S7 shows the simulated k-space oscillations of Ca−Ca and Ca−Zn scattering paths compared to the experimental spectrum of 0.6 mol % Ca/ZnO. The amplitudes of the

oscillations from the Ca−Zn scattering path peak at ∼10 Å^{-1} where the amplitudes of the experimental data approaches zero. However, the convolution of these spectra of paths with similar distances (3.4 Å) reveals a conclusive determination of the influence of the Ca−Zn scattering path on the experimental data. Continuous Cauchy wavelet transform (CCWT) analysis of the EXAFS spectra was performed to deconvolute the *R*-space peak at 3 Å. CCWT analysis demonstrates that there is no difference in the *k*-space oscillation intensity between 1 and 0.6 mol % Ca/ZnO compared to pure CaO (Figure S8). Therefore, there is no detectable scattering from a heavier element. Exploratory simulations of the relaxed CaO cluster supported by ZnO yield an average Ca−Zn distance of 3.43 Å, a coordination number of 3.0, and a static mean-squared relative displacement of 22.4 × 10^{-3} Å^2 (Figure S9). The influence of the ZnO is therefore difficult to observe despite its known presence due to both the low Ca−Zn coordination number and high degree of static disorder at a similar distance to the Ca−Ca interaction. Thus, models with Ca−Zn scattering paths have not been further analyzed. Additionally, models of calcium hydroxide or mixtures of oxide and hydroxide were ruled out due to poor fitting of the data with large *R*-factor, σ^2, and ΔE_0 values (Figures S10, S11 and Tables S6, S7).

3.3. Computational Simulation of X-ray Absorption Spectra of CaO Clusters.
Theoretical simulations of XANES spectra provide additional complementary insight into the specific structures responsible for spectral features observed. The XANES spectra associated with the Ca/ZnO catalysts were simulated using FEFF10, as described in the Methods section. These simulations included consideration of CaO structures organized in multiple spatial arrangements, with separate analyses of Ca atoms in the surface and bulk of three geometries—linear, planar, and cubic—shown in insets of Figure 4. The spectrum of bulk CaO was simulated using a Ca atom surrounded by 6 and 7 full coordination layers for both O and Ca, respectively. This system was used to find the best computational parameters for FEFF and to assess the quality of the XANES simulations for a system with a known structure. The spectrum contains all major features found in the experimental spectrum (Figure S12). Using those parameters, the XANES of a Ca atom on the (100) surface of CaO was also calculated (Figure S13) and found to qualitatively reproduce all the characteristic differing features in the spectrum for a low-Ca-loading catalyst versus bulk CaO—decreased intensity of the shoulder, white line, and EXAFS oscillations as well as increased intensity of a new pre-edge peak. The agreement between the spectrum for 0.6 mol % Ca/ZnO and that simulated for surface atoms supports the existence of clusters with a high fraction of exposed and undercoordinated Ca atoms. Computational investigations into the growth of (CaO)$_n$ clusters found that cubic-like structures, including linear and planar geometries, were most favorable and stable.[46,48,49] Additionally, the experimentally observed Ca−O and Ca−Ca scattering distances of the 0.6 and 1 mol % Ca/ZnO catalysts are consistent with those of bulk CaO. Therefore, unrelaxed clusters with a range of sizes and Ca−Ca coordination numbers were modeled in linear, planar, and cubic geometries (Figure S14) using bulk Ca−O and Ca−Ca distances of 2.41 and 3.40 Å, respectively, as shown in Table 1. The unrelaxed structures provide a convenient, sound approximation because of the negligible differences in the Ca−O bond distance and σ^2 between the experimental bulk

CaO and low-Ca-loading EXAFS fits. The experimentally determined Ca−Ca coordination numbers were 4.1 ± 0.7 and 5.9 ± 0.4 for 0.6 mol % Ca/ZnO and 1 mol % Ca/ZnO catalysts, respectively, which best correspond to linear and planar structures.

Figure S15 shows the average theoretical spectra for each of these structures compared to bulk CaO. Because the main objective is to determine the origin of differences between the low-Ca-loading systems and bulk CaO, the difference spectrum (ΔXANES) between the 0.6 mol % Ca/ZnO catalyst and bulk CaO was generated—it provides a direct visualization of differences in each spectral region. This difference in experimental results was compared to the differences between the theoretical XANES of the linear, planar, and cubic CaO clusters and that of bulk CaO. To provide a more quantitative measure of agreement between theory and experiment, a normalized Frechet distance was calculated as a FOM (Table S8) for the complete theoretical energy range as well as individual ranges that characterize energy regions of importance—pre-edge, shoulder, white line, post-edge, and low EXAFS. The baseline accuracy of the theoretical spectra to the experimental spectra was assessed by applying the Frechet analysis to the experimental versus theoretical CaO bulk data. We find that the largest deviations between theory and experiment (Table S8, bottom) occur in the shoulder and white line regions of the spectra. This is likely due to the use of the muffin-tin potential approximation in FEFF. Therefore, these regions should be considered less relevant when the ΔXANES results are analyzed.

Visual inspection of the ΔXANES results shows the spectra generated from linear clusters ranging from 7.2 to 26.5 Å in length in Figure 4 agree most closely with the experimental spectra in the post-white line and low EXAFS regions, showing little difference for different cluster sizes. The longer linear clusters also give reasonable results in the shoulder region. However, all linear clusters display significant discrepancies relative to the experiment in the pre-edge and white line regions. The Frechet FOM supports this qualitative assessment, showing that the linear clusters provide the best quantitative results in the post-white line region and near-best results in the low EXAFS region. Despite the visual discrepancies in the white line region, the long linear clusters provide the best results in these regions of all clusters studied. Similar agreement and discrepancies with respect to experiment are observed for the planar clusters with side length of 7.2−26.5 Å, but with slightly better agreement in the pre-edge and shoulder region (Figure 4b). Thus, these clusters provide the best overall agreement for all shapes and sizes simulated here. Simulated spectra for cubic clusters begin to resemble those of simulated and experimental bulk CaO, notably in the post-white line and EXAFS regions of the spectra (Figure 4c). Despite providing the best agreement in the pre-edge region, discussed in more detail below, they show an overall less satisfactory agreement than spectra simulated based on the linear and planar structure. Thus, if present, they can be regarded as a minority species. In summary, this analysis suggests that the simulated spectra generated from larger linear and planar structures agree best with experimental results. With these data, it is not possible to definitively conclude which of these structures with low dimensionality is the majority species present in these catalysts because each produces spectra with similarities to experimental results in different spectral regions. Without privileging specific spectral
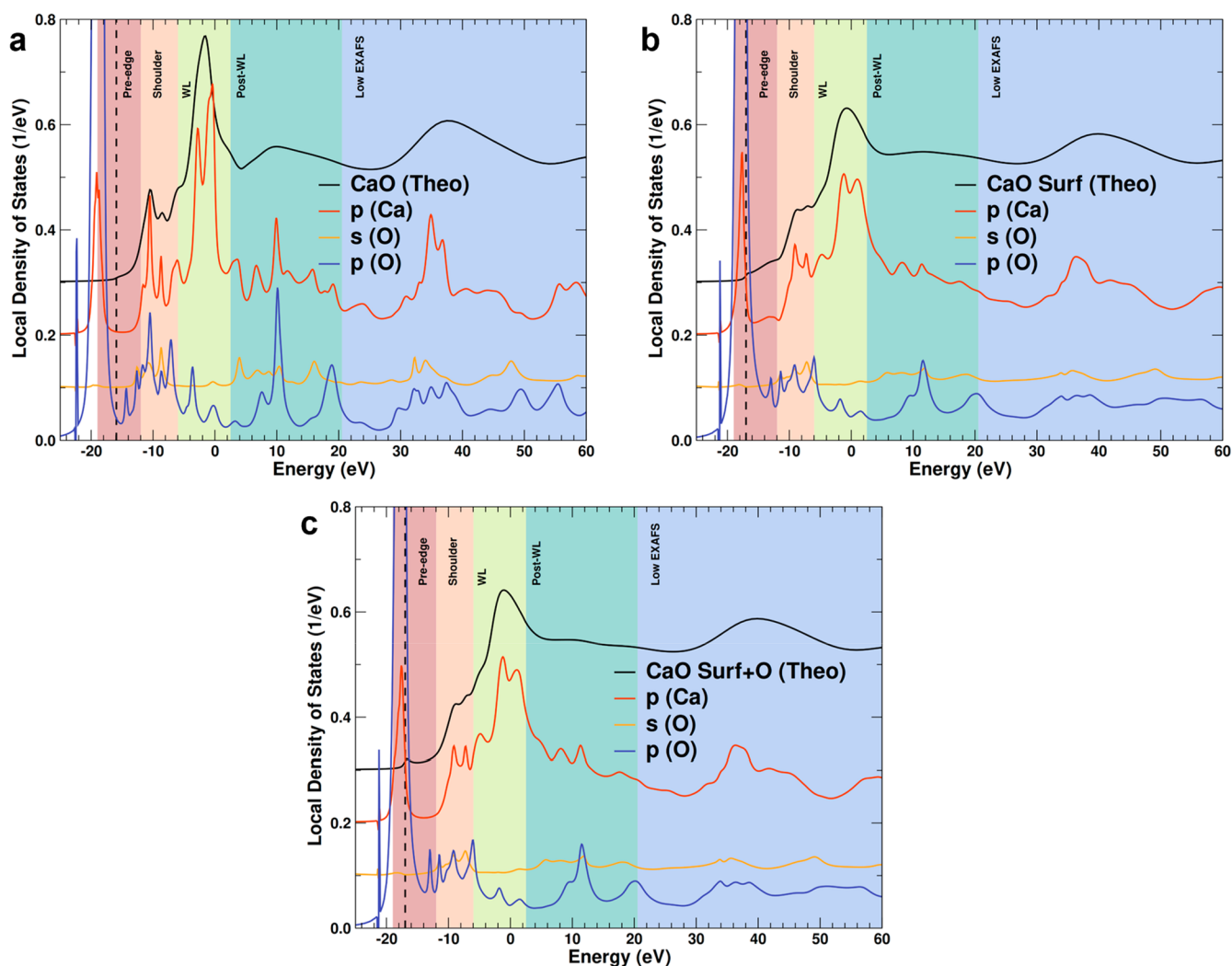
Figure 5. Projected local density of states for (a) bulk CaO, (b) surface Ca atoms, and (c) oxygen-terminated surface Ca atom. The dashed line represents the Fermi level.

regions in the assessment of structures, the results suggest that a mixture of these ultrasmall supported one- and two-dimensional CaO clusters is likely.

The angular momentum decomposed local density of state (LDOS), shown in Figure 5, helps to qualitatively identify which electronic transitions contribute to each region of the spectra. Given the computational cost of the LDOS simulations, here we use Ca on the surface as a proxy for the behavior of undercoordinated atoms in the clusters. In bulk CaO, the white line is dominated by transitions to Ca 4p states, in agreement with selection rules and previous assignments.[50] The shoulder and post-white line regions show clear Ca p−O p hybridization, reflecting oxygen ligation. No electronic transition in the pre-edge region is observed. The LDOS for a surface Ca atom demonstrates hybridization with oxygen p states in the shoulder and post-white line regions, as observed for bulk CaO, but also with much lower intensity. In the LDOS for surface Ca atoms, a pre-edge feature arising from Ca p states is found to exist, likely due to empty p states formed from reduced coordination. When the surface Ca atom is fully coordinated by the addition of a single oxygen atom (Figure 5c), the pre-edge feature disappears, likely due to the conversion and shift to higher energies of the empty p-like

surface state into a σ^* state associated with the new CaO bond. This pre-edge peak has been reported to be the Ca 1s to 3d transition of asymmetric clusters,[39,51] an assumption taken from the interpretation of 3d transition metals. However, Figure 5 demonstrates that the pre-edge can result from the Ca p states of undercoordinated surface Ca atoms. Simulations of the 1s to 3d transition required the activation of quadrupole transitions. Figure S16 deconvolutes the influence of the 1s to p and 1s to d transitions on the LDOS. The 1s to d transition has a negligible contribution to the rise of the pre-edge peak in the undercoordinated surface Ca atom. Geometric distortions around the central absorbing Ca atom do not increase the intensity of the 1s to d transition (Figure S16b,d,f). The LDOS and the weight of the quadrupole transitions suggest the pre-edge peak results from the empty Ca p states in under-coordinated Ca for the unrelaxed structures simulated here. This analysis of the pre-edge peak must be carefully reconciled with the fact that the EXAFS best fit is obtained with fully O-coordinated Ca. Therefore, it is possible that the too large pre-edge peaks observed for the linear and planar clusters compared to the experimental result are due to the presence of too many undercoordinated atoms in these systems, and better results might be obtained by partially capping them.

Altogether, computational analysis of XANES data suggests that catalysts with 1 mol % Ca or less are composed of ultrasmall supported CaO clusters organized into linear and planar atomic structures with monolayer thickness.

3.4. Initial CaO Cluster Speciation Affects CO_2-OCM Performance. Evaluation of the CO_2-OCM performance of these catalysts, reported previously, showed that selectivity to methane coupling was significantly greater for catalysts with less than 2 mol % Ca compared with those with higher Ca loadings.[21] In the low-loading regime, increased Ca loading was associated with increased C_2 product yields. The further observation that the rate of methane coupling normalized by Ca loading was similar among low-loading samples suggested that in the low-loading regime, C_2 production rate increases with an increase in the number of interface sites between CaO and ZnO. At and above 2 mol % Ca loading, further Ca addition only slows the production rate of C_2 species due to the formation of an inactive bulk CaO phase. Characterization by adsorption FTIR revealed that the low loading catalysts were electronically distinct from bulk CaO, likely due to increased interaction with ZnO.[21]

The XAS results reported here validate the previous hypothesis that the Ca species present in the low-loading catalysts are highly dispersed as ultrasmall clusters. As the Ca loading increases, the cluster size becomes slightly larger. Increasing the size of linear and planar CaO structures decreases the amount of the exposed ZnO surface, blocking sites unselective to coupling and creating new, highly selective interfacial sites. For an equivalent number of atoms, the fraction of CaO−ZnO interfacial atomic sites is considerably higher for linear and planar structures than that for the cubic structure. The undercoordinated Ca species present in the clusters, as suggested to exist by the presence of the pre-edge feature, may also serve as selective methane coupling sites independent of the ZnO interaction.[52,53]

3.5. Relating CaO Structure to N_2O-OCM Performance and Kinetics. The Ca/ZnO catalysts with varying Ca loadings were evaluated in this study for their N_2O-assisted methane coupling (N_2O-OCM) activity, which complements our prior catalysis results for CO_2-OCM.[21] Hydrocarbon products observed include ethane, ethylene, propane, propylene, and trace butanes and butenes. As was observed for CO_2-OCM catalysis, it is revealed that there are two regimes of catalytic activity, defined by Ca loading: below 2 mol % Ca, where C_2 product selectivity is 39 ± 1%, and higher Ca loadings, where C_2 product selectivity decreases with Ca loading to only 3% over pure CaO. The transition between these two catalytic regimes correlates with the changes in Ca structure observed by XAS. The catalysts with low-Ca-loading that display higher selectivity to C_2 products were found to be consistent with the coordination environments of ultrasmall linear and planar CaO clusters, while the less-selective catalysts were consistent with those of bulk CaO phases. The distinct activity in the low-loading regime is reflected in Figure 6 by the increase in both selectivity and yield of C_2 products between 0.2 and 0.4 mol % Ca loading; this is the composition range where C_2 product yields begin to increase during CO_2-OCM.[21] At the lowest Ca loading examined, 0.2 mol %, the presence of Ca on the surface had only a minor influence on N_2O-OCM catalysis. However, further addition of linear and planar CaO structures can quickly cover the catalyst surface with selective sites, reflected in the strong influence of loading on performance. Normalizing the activity shown in Figure 6 of
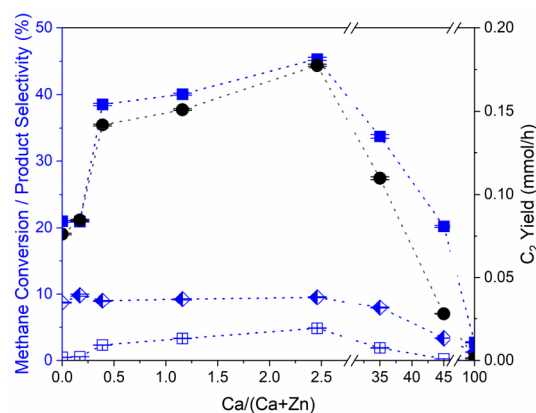

Figure 6. Effects of Ca loading on methane conversion (blue diamond, left half solid), C_2 selectivity (blue solid square), $C_{3,4}$ selectivity (blue open square), and C_2 yield (black solid circle). Reaction conditions: 550 °C; 0.75 g of catalyst; 13.3 mL min^{-1} total gas flow rate with p_{CH_4} = 0.23 atm, p_{N_2O} = 0.45 atm, p_{Ar} = 0.32 atm; average steady-state values with error calculated with 95% confidence interval. All Ca loadings are reported in molar concentrations of metal cations, as determined by ICP-OES (Table S2). All reactant conversions and product yields are reported in Table S9. Dotted lines are included to guide the eye.

the supported cluster catalysts by the mass of Ca, as determined by ICP, results in normalized C_2 product yields of 98 and 35 mmol/h/g_{Ca} over the 1 mol % Ca/ZnO and 0.4 mol % Ca/ZnO catalysts, respectively. The low dimensionality of the CaO clusters implies that nearly all of the Ca atoms are surface-exposed. The normalized C_2 product yield decreases as the cluster sizes become larger, which correlates with the decreasing concentration of undercoordinated Ca atoms associated with increasing cluster size, reflected by the decreasing pre-edge feature. C_{3+} yields shown in Table S9 trend with those of the C_2 products. These higher hydrocarbons are likely secondary products formed by further coupling of C_2 species.[54] Catalysts with ≥35 mol % Ca where large, bulk CaO particles exist have reduced methane coupling performance with increasing loading. Partial or complete combustion to CO_x is favored with increasing loading (Table S9) as the catalyst surface becomes more covered by bulk CaO particles; activity resembles that of pure CaO at the highest loadings.[52,55] The trends of selectivity and product yields for N_2O-OCM are strongly correlated, suggesting that methane oxidation is in direct competition with methane coupling (presumably with the release of methyl radicals[56]) over these catalysts, an observation that is in contrast with findings from CO_2-OCM catalysis, where bulk CaO phases were inactive due to stable carbonate formation.

Direct comparisons of reaction outcomes between CO_2-OCM[21] with N_2O-OCM over Ca/ZnO catalysts are complicated by their differing reaction conditions. In general, lower methane coupling selectivities were observed during N_2O-OCM than those during CO_2-OCM. However, much higher reactor temperatures are necessary for CO_2-OCM due to the high degree of stable $CaCO_3$ formation as well as the high endothermicity associated with that reaction. At present, this trade-off prevents a conclusive determination of which reaction system achieved better methane coupling performance. Instead, the data illustrate the versatility of the Ca/ZnO catalyst system and the strong influence of calcium active site

structure on methane coupling performance in multiple reactive systems.

Analyses of results from XAS and reactor studies establish that there are distinct regimes of both CaO structure and catalytic activity as Ca loading is varied. The impact of the two structural and catalytic regimes—methane coupling-selective small CaO clusters and unselective bulk CaO particles—on reaction kinetics was further studied by comparing the activation energies of 1 mol % Ca/ZnO and 35 mol % Ca/ZnO (Figure 7). Plots of reactant conversion and product
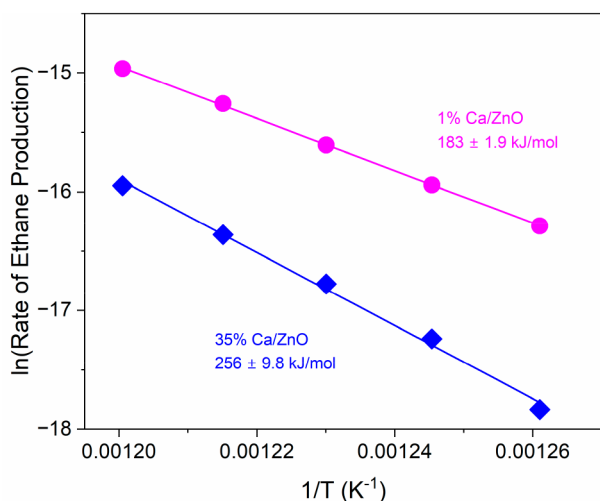

Figure 7. Comparison of activation energies for methane coupling to ethanes over 1 mol % Ca/ZnO and 35 mol % Ca/ZnO: 200 mg of catalyst, total flow of 30 mL/min, $CH_4:N_2O:Ar$ feed ratio of 1:2:1, temperature range of 520−560 °C. Error is calculated from a linear fit.

yields versus inverse space velocity in Figure S17 confirm that the reactor is operating in the differential regime. The activation energies for ethane formation, the primary product of methane coupling, are 183 ± 1.9 and 256 ± 9.8 kJ/mol for 1 mol % Ca/ZnO and 35 mol % Ca/ZnO, respectively. The activation energy of 183 kJ/mol is in good agreement with that previously reported for a similar reactant composition over Li/MgO, where oxygen incorporation from N_2O to the catalyst surface was determined to be the rate-determining step.[54] The significantly larger E_a of 35 mol % Ca/ZnO suggests either a different active site structure, a change in the rate-determining step, or both. The initial CaO structures differ based on the XAS results here, with undercoordinated Ca sites in 1−2D clusters only existing in the low-Ca-loading catalysts. For basic metal oxide catalysts, the presence of CO_2 from reaction products can inhibit methane coupling, shifting the E_a to higher energy due to the formation of carbonate species.[53,54,57] Carbonate can poison CaO active sites and will require higher temperatures to desorb on the high-Ca-loading Ca/ZnO catalysts.[21] Therefore, the higher E_a over the catalyst with a bulk CaO phase is due to a different active site structure that is associated with a different rate-determining step than catalysis with the structure present in 1 mol % Ca/ZnO.

Bulk CaO is very effective at N_2O decomposition to N_2 and O_2.[58−60] N_2O decomposition rates are completely unaffected by the presence of methane over CaO,[61] supporting our finding that bulk CaO does not perform N_2O-OCM but facilitates N_2O decomposition and secondary oxidation reactions. During N_2O decomposition, surface oxygen species

are formed as intermediates in the reaction path leading to desorbed O_2.[62,63] Various adsorbed oxygen species have been found responsible for the overoxidation of methane and hydrocarbon products during OCM.[64,65] The surface species formed on CaO during N_2O decomposition can interact strongly with the hydrocarbons present, leading to eventual oxidation. Gas-phase oxidation to CO_x species can also occur via $CH_3\bullet$ oxidation by molecular O_2.[66] Therefore, the ethane observed to be generated over 35 mol % Ca/ZnO is hypothesized to be a result of the reaction occurring at interfacial sites between CaO and ZnO.

The generation of CO_2 leads to the formation of a stable $CaCO_3$ phase at the reaction temperature.[53] While CaO is still the dominant phase in Ca/ZnO catalysts after N_2O-OCM, the carbonate phase can be observed by XRD on all catalysts with ≥ 1 mol % Ca content after N_2O-OCM (Figure S18). However, pure CaO is converted mostly to carbonate. $CaCO_3$ is a poor N_2O decomposition catalyst.[67] Figure S19 compares the activity of CaO and $CaCO_3$. The conversion of N_2O over CaO is initially 100% and gradually decreases with time on stream as carbonate surface species form. The steady-state C_2 product selectivity over CaO and $CaCO_3$ are 3% and 14%, respectively. Calcium carbonate formation on bulk CaO therefore does not significantly improve the methane coupling performance but inhibits the decomposition of N_2O decomposition. Higher C_2 product selectivities are observed over ZnO-supported CaO clusters than over bulk CaO or $CaCO_3$ catalysts. While carbonate deposition likely occurs on supported CaO clusters during reaction, these catalysts maintain their enhanced methane coupling performance relative to bulk CaO. Neither the rate of carbonate deposition nor any potential *in situ* evolution of CaO during reaction is studied here. All results presented herein indicate the presence of a relationship between the microstructural environment of ZnO-supported Ca in the synthesized catalysts and activity toward methane coupling with alternative oxidants N_2O and CO_2.

4. CONCLUSION

This work investigates the local physical and electronic structures of Ca in ZnO-supported CaO soft-oxidant-assisted methane coupling catalysts through Ca K-edge XANES and EXAFS. XANES results have been interpreted through simulated spectra derived from *ab initio* multiple scattering calculations (FEFF), which elucidate the structural correlates of sites that are active for methane coupling. Results show that below 2 mol % Ca loading, the Ca sites are associated with a coordination environment consistent with CaO clusters organized as one- and two-dimensional structures with approximately one atomic layer thickness. The Ca−Ca coordination numbers derived from EXAFS data suggest that the size of these clusters is approximately 7.2−26.5 Å. The simulated spectrum of a surface Ca atom matches well with the experimental spectrum measured for the low-Ca-loading catalysts. An increasing pre-edge intensity with decreasing Ca loading indicates the presence of undercoordinated surface Ca atoms, according to local densities of states calculations. Catalysts containing these low-dimensional CaO clusters yield enhanced CO_2- and N_2O-assisted methane coupling activity when compared to catalysts containing CaO particles with bulk properties. Significantly different activation energies for ethane formation over 1 mol % Ca/ZnO and 35 mol % Ca/ZnO catalysts are observed (183 ± 1.9 and 256 ± 9.8 kJ/mol,

respectively), which is attributed to observed differences in active site structure and carbonate stability. These results suggest that future investigations of this system should involve *in situ* characterization of the Ca speciation during reactions to probe the significance and influence of carbonate formation on reactivity. These results provide fundamental insights into the active site structure of binary metal oxide catalysts, which contribute to optimization of C_2 product yields during soft-oxidant-assisted methane coupling.

◼ ASSOCIATED CONTENT

ⓢ Supporting Information

The Supporting Information is available free of charge at https://pubs.acs.org/doi/10.1021/acs.jpcc.3c06527.

EXAFS models for S_0^2 determination; EXAFS data of high-Ca-loading catalysts; rejected EXAFS models of $Ca(OH)_2$ and ZnO; wavelet transform analysis; relaxed ZnO-supported CaO cluster structure; simulated XANES spectra of bulk CaO, surface Ca atom, and CaO clusters; Frechet-distance-like error analysis between theory and experiment; summary of N_2O-OCM catalysis results; XRD characterization of spent catalysts (PDF)

◼ AUTHOR INFORMATION

Corresponding Authors

Ron C. Runnebaum − *Department of Chemical Engineering, University of California, Davis, Davis, California 95616, United States; Department of Viticulture & Enology, University of California, Davis, Davis, California 95616, United States;* ⓞ orcid.org/0000-0001-5872-8596; Email: rcrunnebaum@ucdavis.edu

Coleman X. Kronawitter − *Department of Chemical Engineering, University of California, Davis, Davis, California 95616, United States;* ⓞ orcid.org/0000-0002-1240-5027; Email: ckrona@ucdavis.edu

Authors

Leah R. Filardi − *Department of Chemical Engineering, University of California, Davis, Davis, California 95616, United States;* ⓞ orcid.org/0000-0002-0271-7879

Fernando D. Vila − *Department of Physics, University of Washington, Seattle, Washington 98195, United States;* ⓞ orcid.org/0000-0002-6508-4896

Jiyun Hong − *SSRL, SLAC National Accelerator Laboratory, Menlo Park, California 94025, United States;* ⓞ orcid.org/0000-0002-3631-0559

Adam S. Hoffman − *SSRL, SLAC National Accelerator Laboratory, Menlo Park, California 94025, United States;* ⓞ orcid.org/0000-0002-7682-4108

Jorge E. Perez-Aguilar − *SSRL, SLAC National Accelerator Laboratory, Menlo Park, California 94025, United States*

Simon R. Bare − *SSRL, SLAC National Accelerator Laboratory, Menlo Park, California 94025, United States;* ⓞ orcid.org/0000-0002-4932-0342

Complete contact information is available at:
https://pubs.acs.org/10.1021/acs.jpcc.3c06527

Notes

The authors declare no competing financial interest.

◼ ACKNOWLEDGMENTS

◼ REFERENCES

(1) Howarth, R. W. Methane Emissions and Climatic Warming Risk from Hydraulic Fracturing and Shale Gas Development: Implications for Policy. *Energy Emiss. Control Technol.* **2015**, 3, 45−54.

(2) Franz, R.; Uslamin, E. A.; Pidko, E. A. Challenges for the Utilization of Methane as a Chemical Feedstock. *Mendeleev Commun.* **2021**, 31 (5), 584−592.

(3) Chen, W.; Duan, X.; Zhou, X.; Chen, D. Design and Tailoring of Advanced Catalytic Process for Light Alkanes Upgrading. *EcoMat* **2021**, 3 (2), No. e12095.

(4) Horn, R.; Schlögl, R. Methane Activation by Heterogeneous Catalysis. *Catal. Lett.* **2015**, 145 (1), 23−39.

(5) Ortiz-Bravo, C. A.; Chagas, C. A.; Toniolo, F. S. Oxidative Coupling of Methane (OCM): An Overview of the Challenges and Opportunities for Developing New Technologies. *J. Nat. Gas Sci. Eng.* **2021**, 96, 104254.

(6) Ghose, R.; Hwang, H. T.; Varma, A. Oxidative Coupling of Methane Using Catalysts Synthesized by Solution Combustion Method: Catalyst Optimization and Kinetic Studies. *Appl. Catal. A: Gen.* **2014**, 472, 39−46.

(7) Cruellas, A.; Bakker, J. J.; van Sint Annaland, M.; Medrano, J. A.; Gallucci, F. Techno-Economic Analysis of Oxidative Coupling of Methane: Current State of the Art and Future Perspectives. *Energy Convers. Manag.* **2019**, 198, 111789.

(8) Aika, K. I.; Nishiyama, T. Utilisation of CO_2 in the Oxidative Coupling of Methane over PbO-MgO and PbO-CaO. *J. Chem. Soc., Chem. Commun.* **1988**, No. 1, 70−71.

(9) Ayodele, B. V.; Mustapa, S. I.; Witoon, T.; Kanthasamy, R.; Zwawi, M.; Owabor, C. N. Radial Basis Function Neural Network Model Prediction of Thermo-Catalytic Carbon Dioxide Oxidative Coupling of Methane to C_2-Hydrocarbon. *Top Catal.* **2021**, 64, 328−337.

(10) Hutchings, G. J.; Scurrell, M. S.; Woodhouse, J. R. The Role of Surface O^{--} in the Selective Oxidation of Methane. *J. Chem. Soc., Chem. Commun.* **1987**, No. 18, 1388−1389.

(11) Aydin, Z.; Zanina, A.; Kondratenko, V. A.; Rabeah, J.; Li, J.; Chen, J.; Li, Y.; Jiang, G.; Lund, H.; Bartling, S.; et al. Effects of N_2O and Water on Activity and Selectivity in the Oxidative Coupling of Methane over Mn-Na_2WO_4/SiO_2: Role of Oxygen Species. *ACS Catal.* **2022**, 12 (2), 1298−1309.

(12) Istadi; Amin, N. A. S. Synergistic Effect of Catalyst Basicity and Reducibility on Performance of Ternary CeO_2-Based Catalyst for CO_2-OCM to C_2 Hydrocarbons. *J. Mol. Catal. A Chem.* **2006**, 259, 61−66.

(13) Wang, Y.; Ohtsuka, Y. CaO-ZnO Catalyst for Selective Conversion of Methane to C₂ Hydrocarbons Using Carbon Dioxide as the Oxidant. *J. Catal.* **2000**, *192* (1), 252−255.

(14) Wang, Y.; Takahashi, Y.; Ohtsuka, Y. Carbon Dioxide as Oxidant for the Conversion of Methane to Ethane and Ethylene Using Modified CeO₂ Catalysts. *J. Catal.* **1999**, *186* (1), 160−168.

(15) Asami, K.; Fujita, T.; Nishiyama, Y.; Ohtsuka, Y. Formation of Ethane and Ethylene from Methane and Carbon Dioxide over Manganese Oxide Catalysts. *J. Jpn. Pet. Inst.* **1996**, *39* (2), 137−143.

(16) Asami, K.; Fujita, T.; Kusakabe, K.-I.; Nishiyama, Y.; Ohtsuka, Y. Conversion of Methane with Carbon Dioxide into C₂ Hydrocarbons over Metal Oxides. *Appl. Catal. A: Gen.* **1995**, *126* (2), 245−255.

(17) Cai, Y.; Chou, L.; Li, S.; Zhang, B.; Zhao, J. Selective Conversion of Methane to C₂ Hydrocarbons Using Carbon Dioxide over Mn-SrCO₃ Catalysts. *Catal. Lett.* **2003**, *86* (4), 191−195.

(18) Wang, Y.; Zhuang, Q.; Takahashi, Y.; Ohtsuka, Y. Remarkable Enhancing Effect of Carbon Dioxide on the Conversion of Methane to C₂ Hydrocarbons Using Praseodymium Oxide. *Catal. Lett.* **1998**, *56*, 203−206.

(19) Litawa, B.; Michorczyk, P.; Ogonowski, J. Influence of CO₂ on the Catalytic Performance of La₂O₃/CeO₂ and CaO/CeO₂ Catalysts in the Oxidative Coupling of Methane. *Polym. J. Chem. Technol.* **2013**, *15* (1), 22−26.

(20) Ferreira, A. C.; Gasche, T. A.; Leal, J. P.; Branco, J. B. Methane Activation with Nitrous Oxide over Bimetallic Oxide Ca-Lanthanide Nanocatalysts. *Mol. Catal.* **2017**, *443*, 155−164.

(21) Filardi, L. R.; Yang, F.; Guo, J.; Kronawitter, C. X.; Runnebaum, R. C. Surface Basicity Controls C-C Coupling Rates during Carbon Dioxide-Assisted Methane Coupling over Bifunctional Ca/ZnO Catalysts. *Phys. Chem. Chem. Phys.* **2023**, *25* (14), 9859−9867.

(22) Chen, L. X.; Rajh, T.; Wang, Z.; Thurnauer, M. C. XAFS Studies of Surface Structures of TiO₂ Nanoparticles and Photocatalytic Reduction of Metal Ions. *J. Phys. Chem. B* **1997**, *101*, 10688−10697.

(23) Romanchuk, A.; Trigub, A.; Plakhova, T.; Kuzenkova, A.; Svetogorov, R.; Kvashnina, K.; Kalmykov, S. Effective Coordination Numbers from EXAFS: General Approaches for Lanthanide and Actinide Dioxides. *J. Synchrotron Radiat.* **2022**, *29* (2), 288−294.

(24) Karim, A. M.; Prasad, V.; Mpourmpakis, G.; Lonergan, W. W.; Frenkel, A. I.; Chen, J. G.; Vlachos, D. G. Correlating Particle Size and Shape of Supported Ru/γ-Al₂O₃ Catalysts with NH₃ Decomposition Activity. *J. Am. Chem. Soc.* **2009**, *131* (34), 12230−12239.

(25) Yamashita, H.; Nomura, M.; Tomita, A. Local Structures of Metals Dispersed on Coal. 4. Local Structure of Calcium Species on Coal after Heat Treatment and CO₂ Gasification. *Energy Fuels* **1992**, *6* (5), 656−661.

(26) Huggins, F. E.; Huffman, G. P.; Shah, N.; Jenkins, R. G.; Lytle, F. W.; Greegor, R. B. Further EXAFS Examination of the State of Calcium in Pyrolysed Char. *Fuel* **1988**, *67* (7), 938−941.

(27) Okasinski, J.; Cohen, J. B.; Hwang, J.; Mason, T. O.; Ding, Z.; Warschkow, O.; Ellis, D. E. Defect and Electronic Structures of Calcium-Doped Lanthanum Cuprate. *J. Am. Ceram. Soc.* **1999**, *82* (9), 2451−2459.

(28) Liou, S.-C.; Chen, S.-Y.; Lee, H.-Y.; Bow, J.-S. Structural Characterization of Nano-Sized Calcium Deficient Apatite Powders. *Biomater.* **2004**, *25* (2), 189−196.

(29) Qiao, L.; Zizak, I.; Zaslansky, P.; Ma, Y. The Crystallization Process of Vaterite Microdisc Mesocrystals via Proto-Vaterite Amorphous Calcium Carbonate Characterized by Cryo-X-Ray Absorption Spectroscopy. *Crystals* **2020**, *10* (9), 750.

(30) Mirghiasi, Z.; Bakhtiari, F.; Darezereshki, E.; Esmaeilzadeh, E. Preparation and Characterization of CaO Nanoparticles from Ca(OH)₂ by Direct Thermal Decomposition Method. *J. Ind. Eng. Chem.* **2014**, *20* (1), 113−117.

(31) Ravel, B.; Newville, M. ATHENA, ARTEMIS, HEPHAESTUS: Data Analysis for X-Ray Absorption Spectroscopy Using IFEFFIT. *J. Synchrotron Radiat.* **2005**, *12* (4), 537−541.

(32) Jain, A.; Ong, S. P.; Hautier, G.; Chen, W.; Richards, W. D.; Dacek, S.; Cholia, S.; Gunter, D.; Skinner, D.; Ceder, G.; Persson, K. A.; et al. Commentary: The Materials Project: A Materials Genome Approach to Accelerating Materials Innovation. *APL Mater.* **2013**, *1* (1), 11002.

(33) Newville, M. Larch: An Analysis Package for XAFS and Related Spectroscopies. *J. Phys. Conf. Ser.* **2013**, *430* (1), 012007.

(34) Rehr, J. J.; Kas, J. J.; Prange, M. P.; Sorini, A. P.; Takimoto, Y.; Vila, F. Ab Initio Theory and Calculations of X-Ray Spectra. *C. R. Phys.* **2009**, *10* (6), 548−559.

(35) Rehr, J. J.; Kas, J. J.; Vila, F. D.; Prange, M. P.; Jorissen, K. Parameter-Free Calculations of X-Ray Spectra with FEFF9. *Phys. Chem. Chem. Phys.* **2010**, *12* (21), 5503−5513.

(36) Kas, J. J.; Vila, F. D.; Pemmaraju, C. D.; Tan, T. S.; Rehr, J. J. Advanced Calculations of X-Ray Spectroscopies with FEFF10 and Corvus. *J. Synchrotron Radiat.* **2021**, *28* (6), 1801−1810.

(37) Wyckoff, R. W. G. *Crystal Structures*, 2nd ed.; Interscience Publishers: New York, 1963; Vol. *1*.

(38) Lim, Y. S.; Jeong, J. S.; Bang, J.; Kim, J. CaO Buffer Layer for the Growth of ZnO Thin Film. *Solid State Commun.* **2010**, *150* (9−10), 428−430.

(39) Eichert, D.; Salomé, M.; Banu, M.; Susini, J.; Rey, C. Preliminary Characterization of Calcium Chemical Environment in Apatitic and Non-Apatitic Calcium Phosphates of Biological Interest by X-Ray Absorption Spectroscopy. *Spectrochim. Acta, Part B* **2005**, *60* (6), 850−858.

(40) Asokan, K.; Jan, J. C.; Chiou, J. W.; Pong, W. F.; Tseng, P. K.; Lin, I. N. X-Ray Absorption Spectroscopy Studies of Ba₁₋ₓCaₓTiO₃. *J. Synchrotron Radiat.* **2001**, *8*, 839−841.

(41) Chakraborty, D.; Smitshuysen, T. E. L.; Kakekhani, A.; Jespersen, S. P. F.; Banerjee, S.; Krabbe, A.; Hagen, N.; Silva, H.; Just, J.; Damsgaard, C. D.; et al. Reversible Atomization and Nano-Clustering of Pt as a Strategy for Designing Ultra-Low-Metal-Loading Catalysts. *J. Phys. Chem. C* **2022**, *126* (38), 16194−16203.

(42) Tröger, L.; Arvanitis, D.; Baberschke, K.; Michaelis, H.; Grimm, U.; Zschech, E. Full Correction of the Self-Absorption in Soft-Fluorescence Extended X-Ray-Absorption Fine Structure. *Phys. Rev. B* **1992**, *46* (6), 3283−3289.

(43) Jalilehvand, F.; Spångberg, D.; Lindqvist-Reis, P.; Hermansson, K.; Persson, I.; Sandström, M. Hydration of the Calcium Ion. An EXAFS, Large-Angle X-Ray Scattering, and Molecular Dynamics Simulation Study. *J. Am. Chem. Soc.* **2001**, *123* (3), 431−441.

(44) Sowrey, F. E.; Skipper, L. J.; Pickup, D. M.; Drake, K. O.; Lin, Z.; Smith, M. E.; Newport, R. J. Systematic Empirical Analysis of Calcium-Oxygen Coordination Environment by Calcium K-Edge XANES. *Phys. Chem. Chem. Phys.* **2004**, *6*, 188−192.

(45) Batra, P.; Gaba, R.; Issar, U.; Kakkar, R. Structures and Stabilities of Alkaline Earth Metal Oxide Nanoclusters: A DFT Study. *J. Theor. Chem.* **2013**, *2013*, 1−14.

(46) Malliavin, M.-J.; Coudray, C. Ab Initio Calculations on (MgO)ₙ, (CaO)ₙ, and (NaCl)ₙ Clusters (n = 1−6). *J. Chem. Phys.* **1997**, *106* (6), 2323−2330.

(47) Moscovici, J.; Michalowicz, A.; Decker, S.; Lagadic, I.; Latreche, K.; Klabunde, K. Alkaline Earth Oxide Nanoparticles as Destructive Absorbents for Environmental Toxins. *J. Synchrotron Radiat.* **1999**, *6*, 604−606.

(48) Bawa, F.; Panas, I. Competing Pathways for MgO, CaO, SrO, and BaO Nanocluster Growth. *Phys. Chem. Chem. Phys.* **2002**, *4* (1), 103−108.

(49) Aguado, A.; López, J. M. Structures and Stabilities of CaO and MgO Clusters and Cluster Ions: An Alternative Interpretation of the Experimental Mass Spectra. *J. Phys. Chem. B* **2000**, *104* (35), 8398−8405.

(50) Chaboy, J.; Quartieri, S. X-Ray Absorption at the Ca K Edge in Natural-Garnet Solid Solutions: A Full-Multiple-Scattering Investigation. *Phys. Rev. B* **1995**, *52* (9), 6349−6357.

(51) Martin-Diaconescu, V.; Gennari, M.; Gerey, B.; Tsui, E.; Kanady, J.; Tran, R.; Pécaut, J.; Maganas, D.; Krewald, V.; Gouré, E.;

et al. Ca K-Edge XAS as a Probe of Calcium Centers in Complex Systems. *Inorg. Chem.* **2015**, *54* (4), 1283−1292.

(52) Roguleva, V. G.; Kondratenko, E. V.; Maksimov, N. G.; Selyutin, G. E.; Anshits, A. G. The Influence of the Reaction Medium of Oxidative Methane Coupling on the Nature of Bulk Defects of the Li/CaO System. *Catal. Lett.* **1992**, *16* (1), 165−171.

(53) Thum, L.; Rudolph, M.; Schomäcker, R.; Wang, Y.; Tarasov, A.; Trunschke, A.; Schlögl, R. Oxygen Activation in Oxidative Coupling of Methane on Calcium Oxide. *J. Phys. Chem. C* **2019**, *123* (13), 8018−8026.

(54) Yamamoto, H.; Chu, H. Y.; Xu, M.; Shi, C.; Lunsford, J. H. Oxidative Coupling of Methane over a Li^+/MgO Catalyst Using N_2O as an Oxidant. *J. Catal.* **1993**, *142* (1), 325−336.

(55) Roguleva, V. G.; Nikiphorova, M. A.; Maksimov, N. G.; Anshits, A. G. Oxidative Coupling of Methane over Li/CaO Catalysts Using O_2 and N_2O as Oxidants. *Catal. Today* **1992**, *13* (2), 219−226.

(56) Driscoll, D. J.; Martir, W.; Wang, J. X.; Lunsford, J. H. Formation of Gas-Phase Methyl Radicals Over MgO. *J. Am. Chem. Soc.* **1985**, *107* (1), 58−63.

(57) Guan, C.; Liu, Z.; Wang, D.; Zhou, X.; Pang, Y.; Yu, N.; van Bavel, A. P.; Vovk, E.; Yang, Y. Exploring the Formation of Carbonates on La_2O_3 Catalysts with OCM Activity. *Catal. Sci. Technol.* **2021**, *11* (19), 6516−6528.

(58) Snis, A.; Miettinen, H. Catalytic Decomposition of N_2O on CaO and MgO: Experiments and Ab Initio Calculations. *J. Phys. Chem. B* **1998**, *102* (14), 2555−2561.

(59) Hu, X.; Wu, L.; Ju, S.; Dong, C.; Yang, Y.; Qin, W. Mechanistic Study of Catalysis on the Decomposition of N_2O. *Environ. Eng. Sci.* **2014**, *31* (6), 308−316.

(60) Wu, L.; Hu, X.; Qin, W.; Dong, C.; Yang, Y. Effect of Sulfation on the Surface Activity of CaO for N_2O Decomposition. *Appl. Surf. Sci.* **2015**, *357*, 951−960.

(61) Satsuma, A.; Maeshima, H.; Watanabe, K.; Suzuki, K.; Hattori, T. Effects of Methane and Oxygen on Decomposition of Nitrous Oxide over Metal Oxide Catalysts. *Catal. Today* **2000**, *63* (2−4), 347−353.

(62) Karlsen, E. J.; Nygren, M. A.; Pettersson, L. G. M. Theoretical Study on the Decomposition of N_2O over Alkaline Earth Metal-Oxides: MgO-BaO. *J. Phys. Chem. A* **2002**, *106* (34), 7868−7875.

(63) Tench, A. J.; Lawson, T.; Kibblewhite, J. F. J. Oxygen Species Adsorbed on Oxides Part 1.-Formation and Reactivity of $(O^-)_s$ on MgO. *J. Chem. Soc., Faraday Trans. 1* **1972**, *68*, 1169−1180.

(64) Lin, C.-H.; Campbell, K. D.; Wang, J.-X.; Lunsford, J. H. Oxidative Dimerization of Methane over Lanthanum Oxide. *J. Phys. Chem.* **1986**, *90* (4), 534−537.

(65) Peil, K. P.; Goodwin, J. G.; Marcelin, G. Surface Phenomena during the Oxidative Coupling of Methane over Li/MgO. *J. Catal.* **1991**, *131* (1), 143−155.

(66) Karakaya, C.; Zhu, H.; Zohour, B.; Senkan, S.; Kee, R. J. Detailed Reaction Mechanisms for the Oxidative Coupling of Methane over La_2O_3/CeO_2 Nanofiber Fabric Catalysts. *ChemCatChem* **2017**, *9* (24), 4538−4551.

(67) Hansen, P. F. B.; Dam-Johansen, K.; Johnsson, J. E.; Hulgaard, T. Catalytic Reduction of NO and N_2O on Limestone during Sulfur Capture under Fluidized Bed Combustion Conditions. *Chem. Eng. Sci.* **1992**, *47* (9−11), 2419−2424.